Properties of Arctic liquid and mixed phase clouds from ship-borne Cloudnet observations during ACSE 2014

Peggy Achtert[1,2], Ewan J. O'Connor[3,4], Ian M. Brooks[1], Georgia Sotiropoulou[5,6], Matthew D. Shupe[7,8], Bernhard Pospichal[9], Barbara J. Brooks[10], and Michael Tjernström[5]

[1]Institute for Climate and Atmospheric Science, School of Earth and Environment, University of Leeds, Leeds, UK
[2]Now at Meteorological Observatory Hohenpeißenberg, German Weather Service, Germany
[3]Finnish Meteorological Institute, Helsinki, Finland
[4]Meteorology Department, University of Reading, Reading, UK
[5]Department of Meteorology and the Bert Bolin Centre for Climate Research, Stockholm University, Stockholm, Sweden
[6]Now at Laboratory of Atmospheric Processes and Their Impacts, School of Architecture, Civil & Environmental Engineering, École Polytechnique Fédérale de Lausanne (EPFL), Lausanne, Switzerland
[7]Cooperative Institute for the Research in Environmental Sciences, University of Colorado Boulder, Boulder, Colorado, USA
[8]Earth System Research Laboratory, National Oceanic and Atmospheric Administration, Boulder, Colorado, USA
[9]Institute for Geophysics and Meteorology, University of Cologne, Cologne, Germany
[10]National Centre for Atmospheric Science, University of Leeds, Leeds, UK

Correspondence: Peggy Achtert (p.tesche-achtert@dwd.de)

Abstract. This study presents Cloudnet retrievals of Arctic clouds from measurements conducted during a three-month research expedition along the Siberian shelf during summer and autumn 2014. During autumn, we find a strong reduction in the occurrence of liquid clouds and an increase for both mixed-phase and ice clouds at low levels compared to summer. About 80% of all liquid clouds observed during the research cruise show a liquid water path below the infra-red black body limit of

5 approximately $50\,\mathrm{gm^{-2}}$. The majority of mixed-phase and ice clouds had an ice water path below $20\,\mathrm{gm^{-2}}$.

Cloud properties are analysed with respect to cloud-top temperature and boundary layer structure. Changes in these parameters have little effect on the geometric thickness of liquid clouds while mixed-phase clouds during warm-air advection events are generally thinner than when such events were absent. Cloud-top temperatures are very similar for all mixed-phase clouds. However, more cases of lower cloud-top temperature were observed in the absence of warm-air advection.

10 Profiles of liquid and ice water content are normalised with respect to cloud base and height. For liquid water clouds, the liquid water content profile reveals a strong increase with height with a maximum within the upper quarter of the clouds followed by a sharp decrease towards cloud top. Liquid water content is lowest for clouds observed below an inversion during warm-air advection events. Most mixed-phase clouds show a liquid water content profile with a very similar shape to that of liquid clouds but with lower maximum values during warm-air advection. The normalised ice water content profiles in mixed-

15 phase clouds look different from that of liquid water content. They show a wider range in maximum values with lowest ice water content for clouds below an inversion and highest values for clouds above or extending through an inversion. The ice water content profile generally peaks at a height below the peak in the liquid water content profile – usually in the centre of the cloud, sometimes closer to cloud base, likely due to particle sublimation as the crystals fall through the cloud.

1 Introduction

Over the past 30 years the rate of Arctic warming has been consistently larger than the global average, by a factor of 2-3 (Stocker, 2014). This has led to a decrease in sea-ice cover and new record minima in the late summer sea-ice extent in the Arctic occurred in 2007 and 2012. The warming of the Arctic prolongs the sea-ice melt season (Markus et al., 2009), which specifically reduces the cover of perennial sea ice (Maslanik et al., 2011). There is not yet a consensus regarding which

25 mechanisms dominate the rapid warming in the Arctic. Although climate models agree on an enhanced Arctic warming, sometimes referred to as the Arctic amplification (Polyakov et al., 2002; Serreze and Francis, 2006; Serreze and Barry, 2011), they largely fail to predict the accelerated retreat of Arctic sea ice (Stroeve et al., 2012). This is at least partly caused by an inadequate description of the processes that control the coupled oceanic-atmospheric energy balance and the feedback mechanisms between sea-ice cover and other components of the Arctic climate system (Liu et al., 2012), particularly clouds.

30 Arctic low- and mid-level clouds can differ significantly from their counterparts at lower latitudes. They are generally long-lived and of mixed-phase nature (Shupe, 2011b) whose macrophysical (base and top altitudes, horizontal extent), microphysical properties (e.g., cloud droplet and ice crystal number concentrations, liquid water path (LWP), ice water path (IWP), and liquid-ice partitioning) and radiative effects are influenced by the low aerosol particle – cloud condensation nuclei (CCN) and ice nucleating particle (INP)– number concentrations during summer (Mauritsen et al., 2011; Birch et al., 2012; Tjernström et al.,

35 2014; Hines and Bromwich, 2017). The aerosol particle size distribution can affect the distributions of, and the feedback between, liquid water and ice particles in the clouds, and thus impact the radiative properties of the clouds (Solomon et al., 2009). In addition, temperature and moisture inversions influence entrainment at cloud top with consequences for cloud development (Sedlar and Tjernström, 2009; Sedlar et al., 2012; Solomon et al., 2011).

The impact of Arctic clouds on solar and terrestrial radiation is not well quantified, and hence the accurate description of

40 the atmospheric and surface energy budgets remains one of the core problems in Arctic climate modelling (Karlsson, 2011; Boeke and Taylor, 2016). Low-level liquid-water and mixed-phased clouds are of particular importance, typically evolving through cloud-top radiative cooling and consequent turbulent mixing and entrainment of warm and humid air. They form in statically stable atmospheric conditions, and persist for extended periods of time. Steele et al. (2010) show that about 60% of the energy that is consumed by the melting sea ice during the melting season is provided by radiative energy or sensible heat

45 fluxes directly from the atmosphere to the surface, both strongly modified by clouds. Hence, even small errors in parameters affecting the downward radiative fluxes absorbed and emitted by clouds, such as cloud cover, microphysical, macrophysical and optical properties (Tjernström et al., 2008; Walsh et al., 2009; Birch et al., 2009, 2012; Hines and Bromwich, 2017), may have far-reaching consequences on the surface energy budget in the Arctic (Sedlar et al., 2011; Bennartz et al., 2013; Ebell et al., 2020), and consequently on ice melt (Tjernström, 2005).

50 Of particular importance is the thermodynamic phase of the clouds in the Arctic as it significantly affects their radiative effect (Shupe and Intrieri, 2004; Choi et al., 2014; Komurcu et al., 2014; Tan et al., 2016). For instance, the widespread occurrence

of warm liquid-water clouds, i.e. clouds with top temperature above 0°C, as identified in remote-sensing observations collected during the Arctic Clouds in Summer Experiment (ACSE) has been associated with observations of rapid decrease in sea-ice cover (Tjernström et al., 2015). A complicating factor is that the properties and behaviour of Arctic boundary-layer clouds may

55 differ with region. For example, a statistical analysis of radiative properties of the clouds observed during ACSE showed that knowledge derived from measurements across the pan-Arctic area and on the central ice-pack does not necessarily apply closer to the ice-edge (Sotiropoulou et al., 2016). In addition, cloudiness and its effect on the energy balance at the surface strongly depends on the change in specific humidity within surface inversions (Tjernström et al., 2019).

This paper continues the investigation of the clouds observed during the ACSE expedition, focussing on their properties as

60 derived from synergetic remote-sensing measurements. Such information is needed to improve the understanding necessary to improve representation of Arctic clouds in global numerical weather prediction and climate models.

2 Measurements and methods

2.1 The field campaign

ACSE was part of the Swedish-Russian-US Arctic Ocean Investigation of Climate-Cryosphere-Carbon Interactions (SWERUS-

65 C3) project. Measurements were made during a 3-month research cruise on the icebreaker Oden, from 3 July to 5 October 2014. The expedition started from Tromsø, Norway, and followed the Siberian Shelf, crossing the Kara, Laptev, East Siberian, and Chukchi Seas to arrive off Barrow, Alaska, on 19 August. Following a change of crew and science teams, Oden returned to Tromsøon a route somewhat to the north of the outbound leg. The cruise track is shown in Figure 1 together with the tracks of research cruises undertaken in two previous projects: the Surface Heat Budget of the Arctic Ocean (SHEBA, Uttal et al.

70 (2002)) and Arctic Summer Cloud Ocean Study (ASCOS, Tjernström et al. (2014)) experiments. One of the primary aims of ACSE was to investigate the effect of different surface conditions (i.e., open water, marginal ice zones, and sea ice) on the macrophysical and microphysical properties of Arctic low- and mid-level clouds through the late summer melt season into the early autumn freeze up.

2.2 Instrumentation and data processing

75 The suite of remote-sensing instruments employed in this study comprise a W-band Doppler cloud radar (National Oceanic and Atmospheric Administration, Boulder, USA), a motion-corrected Doppler wind lidar (HALO Photonics, Achtert et al. (2015)), a laser ceilometer (Vaisala CL31), and a scanning microwave radiometer (Radiometer Physics HATPRO). The W-band cloud radar is a motion-stabilised system developed specifically for shipborne deployments (Moran et al., 2012) operating at 94 GHz and measuring the Doppler spectrum from which the first three moments (reflectivity, Doppler velocity, Doppler spectrum

80 width) are calculated. It is a pulsed system and provides vertical profiles with 31.22 m vertical resolution and 0.5 s temporal resolution. During ACSE, the lowest and highest range gates were set to 80 m and 5980 m, respectively.

The Doppler lidar is a pulsed heterodyne system operating at a wavelength of 1.5 μm and a pulse repetition frequency of 15 kHz. Range resolution was set at 18 m and 30 000 pulses accumulated to achieve a temporal resolution of 2 s. The scan schedule comprised a fixed schedule for the entire voyage of a continuous vertical stare mode interspersed with a five-beam

85 wind scan every 10 minutes at an elevation angle of 70 degrees from horizontal. A full description of the system parameters and scan schedule is given in Achtert et al. (2015). The Doppler lidar signal was corrected following Manninen et al. (2016). This new background correction, developed for measurements in low-aerosol conditions, improves the signal to noise ratio threshold for reliable data by about 4 dB above the original signal threshold(Achtert et al., 2015), increasing data availability and providing more reliable Doppler velocity uncertainty estimates.

90 The ceilometer operates at a wavelength of 905 nm with a vertical resolution of 10 m. Pulses are accumulated to a temporal resolution of 30 s. The instrument and was deployed pointing to zenith.

The microwave radiometer is a RPG-HATPRO-G1, which is a passive system monitoring 14 channels in two frequency bands (7 for humidity profiling and liquid water path retrievals between 22 and 31 GHz; 7 for temperature profiling between 51 and 58 GHz). We retrieve the liquid water path (LWP) from the raw microwave brightness temperature measurements

95 following Löhnert and Crewell (2003) and Massaro et al. (2015). This statistical retrieval requires climatological profiles of pressure, temperature and humidity as derived from soundings. A suitable training data set was assembled from a total of 1826 radiosondes launched in the Arctic Ocean from the research vessels Polarstern (https://data.awi.de/?site=home), Mirai (http://www.godac.jamstec.go.jp/darwin/e), and Oden (https://bolin.su.se/data/) between 1990 and 2014. The soundings were separated according to summer (June, July, August, 1025 radiosondes) and autumn (September, October, 801 radiosondes).

100 LWP measurements are limited to non-precipitating cases as heavy rain can impact the LWP retrieval (Crewell et al., 2003).

Surface meteorology measurements included air temperature, humidity, mean and turbulent winds, visibility, and downwelling solar and infra-red radiation. Radiosondes (Vaisala RS92) were launched four times a day at 0000, 0600, 1200, and 1800 UTC.

These measurements allow for a comprehensive characterisation of clouds using the Cloudnet algorithm (Illingworth et al.,

105 2007), combining cloud radar, ceilometer, microwave radiometer and radiosonde profiles averaged to a common grid at the cloud radar resolution. The radiosonde profiles provide the initial temperature and humidity profiles for Cloudnet. They also supply the information necessary to estimate and correct for gaseous and liquid attenuation of the radar reflectivity. Gaseous attenuation at 94 GHz is not so severe in Arctic conditions but may reach 1 dB already within 2 km, whereas attenuation by liquid cloud layers can reach 2 dB or more. This attenuation, if uncorrected for, would cause a significant bias in derived

110 ice water contents (IWC), especially if occurring above liquid layers. Together with the re-gridded remote-sensing data, the Cloudnet scheme also provides an objective hydrometeor target classification at the same cloud radar resolution; the re-gridded data and the target classification are combined in a single file termed the target categorisation product which also contains the measurement uncertainties for propagation through to all products.

The target categorisation product is the basis for deriving consistent retrievals of cloud occurrence, top and base height, cloud

115 thickness, cloud phase, liquid and ice-water path, liquid and ice water content, and the effective radius of cloud droplets and ice crystals. Liquid water content (LWC) is calculated from microwave radiometer-derived LWP (with an offset correction based

on clear-sky periods) and liquid layer cloud boundaries by distributing the liquid using the scaled-linear adiabatic assumption, i.e. LWC increasing linearly with height from zero at cloud base (Albrecht et al., 1990; Boers et al., 2000). Typical errors in LWC are below 20% (Ebell et al., 2010). IWC is calculated from radar reflectivity and temperature using the method of
120 Hogan et al. (2006), where the fractional error in IWC at 94 GHz is +55%/-35% between -10 and -20 C, rising to +90%/-47% for temperatures below -40°C. Note that an error in the calibration of the radar reflectivity of 1 dB would bias IWC by 15%.

The Cloudnet target classification Illingworth et al. (2007) has been used to separate between water clouds, ice clouds, and mixed-phase clouds on a profile-by-profile basis with a resolution of 30 s, and to identify cloud base and top heights. The original Cloudnet target classification for the three months of ACSE measurements is presented in Figure 2. The figure also
125 shows fog periods as identified by a visibility of less than 1 km in the 10-min mean of the visibility sensor measurements aboard Oden. The target classification reveals an unrealistically high occurrence of *Aerosol*, *Aerosol & insects*, and *Insects* during periods that were actually dominated by fog. Hence, visibility data have been used to re-classify some of the targets originally misidentified by Cloudnet into these categories below 500 m as fog. Cloud profiles are classified as mixed-phase if they show a cloud layer classified as Cloud droplets only but features precipitating ice below cloud base, or if a cloud layer
130 contains regions of any combination of *Ice only*, *Cloud droplets only* and *Ice & super-cooled droplets*. Profiles of cloud fraction per volume (Brooks et al. 2005) have been obtained using time-height sections of 30 min by 90 m height (3 height bins).

We use the estimates of the depth of the planetary boundary layer (PBL) provided by Sotiropoulou et al. (2016). They obtained PBL depths from the locations of the main inversions in the radiosonde temperature profiles following the methodology of Tjernström and Graverson (2009). A separation between coupled and decoupled boundary layers (Shupe et al., 2013;
135 Sotiropoulou et al., 2014; Brooks et al., 2017) was performed by investigating the presence of an additional, weaker, temperature inversion below the main inversion (Sotiropoulou et al., 2016). An absence of such an additional lower inversion defines coupled PBLs. Cloudnet retrievals within one hour of a sounding have been used in the investigation of the effects of (a) coupled and decoupled PBLs and (b) the location of the clouds with respect to the inversion (i.e. PBL top) on the observed cloud properties. To avoid oversampling of persistent clouds, we considered only one Cloudnet profile every 5 minutes, leading to at
140 most 24 profiles for per sounding.

Based on sounding data taken during ACSE, Sotiropoulou et al. (2016) defined the change between summer and autumn by a rapid change in temperature in the lower atmosphere on 28 August 2014. Here, we use this date to investigate changes in the observed cloud properties and occurrence rates between the two seasons. We further separate the large-scale circulation between warm-air advection events (WAA, Tjernström et al. (2015) and conditions during which no warm-air advection took
145 place (non-WAA). WAA was identified from the ACSE soundings as when the temperature at 1.0 km height exceeded a threshold of 5°C, empirically derived from Figure 2a of Sotiropoulou et al. (2016). These events were particularly pronounced during the ACSE summer observations (Tjernström et al., 2015, 2019).

The investigation of clouds in this study is restricted to heights below 6 km, the maximum height of the cloud radar observations during ACSE. For the statistical analysis of the occurrence of different cloud types and cloud layers, we hence include
150 only those clouds that show a cloud-top height below 6 km, considering up to three cloud layers per profile. This means that deep mid-level clouds and cirrus are not fully covered in our data set.

3 Results

3.1 Cloud occurrence

Cloud occurrence probability distributions as a function of height are shown in Figure 3, both for total occurrence and par-
155 titioned into liquid, ice, and mixed-phase clouds for the entire ACSE campaign, and separated into summer and the autumn
seasons following Sotiropoulou et al. (2016). For completeness, the cloud fraction for all clouds, i.e. including those with a
cloud-top height above 6 km for which only cloud base could be detected, is provided as dotted line.

In general, Figure 3 shows that clouds were more abundant below 4 km height during autumn than during summer. This is
reflected in the lower tropospheric maxima of the mean cloud fraction of 0.28 and 0.74 in summer and autumn, respectively. In
160 summer, there is a clear separation between height ranges dominated by liquid-water (< 1.2 km) and by ice clouds (> 1.2 km).
Mixed-phase clouds during summer were found at all height levels though their cloud fraction strongly decreased upwards of
0.5 km. Autumn showed a strong reduction in the occurrence of liquid clouds and an increase in both mixed-phase clouds and
ice clouds at low levels. Ice clouds during autumn extended almost down to the surface, while low clouds during summer were
predominantly liquid.

165 A statistical overview of top temperature, top height, bottom height, and geometrical thickness of the clouds observed during
ACSE is provided in Figure 4. The results refer to cloud layers (up to three allowed per profile) for which both cloud base and
top could be clearly identified. The minimum cloud geometrical depth was defined by the radar range resolution of 31 m.
Again, the results were separated according to cloud phase and season. Average cloud top temperatures were 0°C for liquid
clouds, -10°C for mixed-phase clouds, and -15°C for ice clouds. Cloud top temperatures were slightly higher during summer
170 and slightly lower during winter, though with a similar spread of values. The seasonal behaviour of cloud top and base heights
for liquid clouds differs from that of ice and mixed-phase clouds. Liquid clouds were relatively unchanged in vertical extent
between summer and autumn, while both ice and mixed-phase clouds had lower top and base heights in autumn than in summer.

In general, the clouds observed during ACSE were rather shallow with a median (mean) geometrical thickness of 250 m (800
m). Liquid clouds were found to be thinnest during both seasons and with only a small variation between median (220 m) and
175 mean (285 m) values. Mixed-phase clouds were the thickest with median depths of 750 m and 940 m in summer and winter,
respectively, with a similar mean value for both seasons. Ice clouds were slightly deeper in autumn, with a median (mean)
geometric thickness of 250 m (730 m) compared to 220 m (570 m) in summer. It should be emphasised that these statistics are
dominated by liquid clouds in summer and by mixed-phase clouds during autumn.

3.2 LWP, IWP and cloud top temperature

180 #### 3.2.1 Liquid-water clouds

The frequency distribution of LWP in liquid water clouds during summer and autumn is shown in Figure 5a. While a negative
LWP related to the retrieval error of 25-30 $\mathrm{g\,m^{-2}}$ (Turner, 2007) is clearly unphysical, these values cannot be excluded without
biasing the statistics. Liquid water clouds during summer had a mean LWP of 37±59 $\mathrm{g\,m^{-2}}$ and median of 13 $\mathrm{g\,m^{-2}}$. These

values were similar during autumn with a mean of $41\pm54\,\mathrm{gm}^{-2}$ and median of 20 g/m2. Both distributions peak at a LWP around $10\,\mathrm{gm}^{-2}$. In summer a small number of clouds (less than 1% of all cases) had a LWP in excess of $400\,\mathrm{gm}^{-2}$ while in autumn the maximum LWP was approximately $495\,\mathrm{gm}^{-2}$. These high values of LWP are generally related to frontal passages. Almost no seasonal difference in the LWP distributions is apparent in the cumulative frequency curves in Figure 5a. The curves also show that in summer and autumn 76% and 72%, respectively, of liquid clouds were below the infra-red black body limit of approximately $50\,\mathrm{gm}^{-2}$ (Tjernström et al., 2015). If the black body limit is set to $30\,\mathrm{gm}^{-2}$ (Shupe and Intrieri, 2004), the occurrence rates are reduced to about 67% in summer and 60% in autumn. These clouds were therefore often semi-transparent to long-wave radiation; hence, long-wave cooling and the resulting turbulence generated in cloud, as well as the surface downwelling radiation, will be very sensitive to small changes in LWP.

Figure 5b shows the distribution of cloud-top temperature for liquid-water clouds during summer and autumn. Summer liquid clouds were warmer than those in winter. Their cloud top could be warmer than 15°C but were never found to be colder than -15°C. A closer look at the data revealed that all the cloud-top temperatures above 10°C were the result of a period of strong warm air advection that occurred in the beginning of August (Tjernström et al., 2015, 2019). The cloud-top temperature distribution observed during summer resembles that derived from Cloudnet observations at mid-latitudes (Bühl et al., 2016). In autumn, liquid cloud-top temperatures rarely exceed 0°C with observed values as low as -25°C. The maximum of cloud-top temperature occurrence rate shifts from 0°C in summer to -5°C in autumn. In addition, cloud-top temperatures for autumn also show a broader distribution with a long tail towards low temperatures than those in summer.

3.2.2 Mixed-phase clouds

The LWP frequency distribution for mixed-phase clouds presented in Figure 6a is similar to that for liquid-only clouds in Figure 5a though with a broader shape. Summer had more cases of high LWP and fewer cases of low LWP than autumn. For both seasons, the peak occurrence was at around $10\,\mathrm{gm}^{-2}$. The mean and median values, however, are higher than for liquid-only clouds, with summer values of $98\pm94\,\mathrm{gm}^{-2}$ and $72\,\mathrm{gm}^{-2}$, respectively; in autumn the corresponding values are $34\pm44\,\mathrm{gm}^{-2}$ and $21\,\mathrm{gm}^{-2}$. The cumulative distributions in Figure 6a show that, with infrared-black body limit of $50\,\mathrm{gm}^{-2}$ ($30\,\mathrm{gm}^{-2}$), 41% (31%) and 76% (60%) of the clouds during summer and autumn, respectively, had LWPs below this limit. The same general relationships of higher median LWP in mixed-phase clouds compared with liquid-only clouds is consistent with the observations during SHEBA (Shupe et al., 2006).

In contrast to LWP, there is little difference in the frequency distributions for IWP in the mixed-phase clouds observed in either summer or autumn (Figure 6b). The majority of clouds had an IWP below $20\,\mathrm{gm}^{-2}$ with mean and median values in summer of 34 and $7\,\mathrm{gm}^{-2}$, respectively, and in autumn of 32 and $9\,\mathrm{gm}^{-2}$.

During summer, IWC was lowest in clouds with a low cloud top height and highest for clouds with tops between 3.0 and 4.0 km and cloud-top temperatures of -8°C to -17°C (not shown). During autumn, the lowest values of IWC were observed for clouds with top heights in the range from 2.0 to 3.0 km. Cold clouds with cloud top temperatures between -15°C and -35°C and cloud top heights above 4.0 km had the largest values of IWC (not shown). The majority of mixed-phase clouds

during summer and autumn had very low IWC; $< 0.1\,\mathrm{gm}^{-3}$. Mean (median) values were $0.0156\,\mathrm{gm}^{-3}$ ($0.0025\,\mathrm{gm}^{-3}$) and $0.0087\,\mathrm{gm}^{-3}$ ($0.0016\,\mathrm{gm}^{-3}$) during summer and autumn, respectively.

The frequency distribution of cloud-top temperature in Figure 6c again shows a different behaviour for clouds during summer
220 and autumn. During summer, the tops of mixed-phase clouds were generally warmer than in autumn with a maximum at 0°C
to -2.5°C. However, they were always colder than liquid-only clouds during the same season. During summer, cloud-top
temperature could be as low as -30°C though they were mostly warmer than -5°C. Autumn had a bi-modal distribution of
cloud-top temperature, which could be the result of precipitating (T_{top} >-10°C) versus non-precipitating clouds (T_{top} <-10°C)
(Westbrook and Illingworth, 2011). Very few mixed-phase clouds showed cloud-top temperatures above 0°C (these were cases
225 related to warm-air advection events where the cloud top extended into the warmer air above) or as low as -35°C. In general,
mixed-phase cloud top temperatures were up to 5°C colder during autumn than during summer.

3.2.3 Effect of boundary-layer structure

Here we investigate the effects of PBL structure on the observed clouds. The PBL top is defined as the height of the strongest
temperature inversion (Brooks et al., 2017) within the lowermost $3\,\mathrm{km}$ of the atmosphere (Sotiropoulou et al., 2016). Clouds
230 are considered to be *below* the inversion (cloud top below the PBL top), *above* the inversion (cloud base above the PBL top),
or to *extend into* the inversion (cloud base below PBL top and cloud top above PBL top).

Figure 7 provides a statistical overview of the geometrical thickness and cloud-top temperature of clouds for different PBL
structure and large-scale circulation. We separate between liquid and mixed-phase clouds observed above, below, and extending
into the inversion during WAA and non-WAA conditions as well as for coupled and decoupled PBLs. Cases of liquid and
235 mixed-phase clouds in decoupled PBLs during WAA events were rare (N<100) in the ACSE data set, and thus, not considered
here. Liquid clouds showed little difference in mean and median cloud thickness. However, they do show a clear difference
in the frequency distribution of cloud-top temperature with respect to WAA and non-WAA conditions. Mixed-phase clouds
during WAA were generally thinner than during non-WAA. The deepest mixed-phase clouds were found for non-WAA and
for decoupled PBLs. No difference is found in the thickness (Figure 7b) and cloud-top temperature (dotted line in Figure 7d)
240 of mixed-phase clouds below the inversion for coupled and decoupled PBLs suggesting little difference in the geometrical
properties of those clouds. The frequency distributions of cloud-top temperatures are very similar for all mixed-phase clouds
observed for non-WAA and coupled PBLs, with a broad peak in occurrence between 0°C and -20°C. The cloud-top temperature
distributions are shifted to lower values for decoupled PBLs during non-WAA. In accordance with their decreased geometrical
thickness, mixed-phase clouds during WAA show a maximum in the frequency distribution of cloud-top temperature at higher
245 temperatures; between 5°C and -25°C. The small number of positive cloud-top temperatures during WAA events is the result
of cloud tops extending into the warmer air aloft.

Figure 8 provides a profile view of the LWC and the IWC of the clouds considered in Figure 7. The scaled altitude ranges
from the base of the clouds (zero) to the cloud top (unity). All profiles have been interpolated to intervals of 0.1 scaled altitude.
Liquid clouds show maximum LWC between 0.03 and $2.00\,\mathrm{gm}^{-3}$ within the upper quarter of the cloud. The LWC is lowest
250 for clouds observed below the inversion during WAA. The LWC within mixed-phase clouds shows lower maxima than that of

liquid clouds. Mixed-phase clouds during WAA generally show a lower maximum in LWC compared to those observed during non-WAA.

The profiles of IWC in mixed-phase clouds are distinctly different from those of LWC. They show a wide range in maximum values with lowest IWC close to $0\,\mathrm{g\,m^{-3}}$ for clouds below the inversion and highest values of 0.25 to $0.75\,\mathrm{g\,m^{-3}}$ for clouds
255 above or extending through the inversion. Note that these are also the geometrically thinnest and thickest clouds, respectively (Figure 7). The IWC profile generally peaks at a height below the peak in the LWC profile – usually in the centre of the cloud but sometimes closer to cloud base, likely due to increasing particle sublimation as the crystals fall.

During non-WAA, liquid clouds below the inversion (i.e. with cloud top at or below PBL top) showed no statistically significant difference in LWP (two-sample t-test, $p < 0.05$) for coupled and de-coupled PBLs, with mean values of $24\pm62\,\mathrm{g\,m^{-2}}$
260 (median of $6\,\mathrm{g\,m^{-2}}$) and $22\pm41\,\mathrm{g\,m^{-2}}$ (median of $8\,\mathrm{g\,m^{-2}}$), respectively (not shown). For clouds below the inversion in coupled PBLs, 90% of cases showed LWP below $50\,\mathrm{g\,m^{-2}}$ while this number slightly decreases to 88% for clouds below the inversion in decoupled PBLs. This behaviour is consistent with the observations reported in Sotiropoulou et al. (2016).

Mixed-phase clouds in the same situation (non-WAA, below inversion) showed LWP behaviour for coupled and de-coupled PBLs opposite to that of liquid clouds. We find a statistically significant difference (two-sample t-test, $p < 0.05$) with mean
265 values of $33\pm57\,\mathrm{g\,m^{-2}}$ (median of $13\,\mathrm{g\,m^{-2}}$) and $52\pm63\,\mathrm{g\,m^{-2}}$ (median of $32\,\mathrm{g\,m^{-2}}$), for coupled and de-coupled PBLs, respectively (not shown). For clouds below the inversion in coupled PBLs, 76% of cases showed LWP below $50\,\mathrm{g\,m^{-2}}$ while this number decreased to 64% for clouds below the inversion in decoupled PBLs. Interestingly, mixed-phase clouds below the inversion in decoupled PBLs were slightly thinner than in coupled PBLs (Figure 7b) while little difference was found in their respective profiles of IWC (Figure 8c).

270 **4   Discussion**

Cloud observations in the Arctic are scarce. Available data sets are from different geographic regions, represent different time periods, and were obtained using different retrieval methods. Consequently, care must be taken when comparing them. Additional constraints apply when also considering spaceborne cloud observations. For instance, the CloudSat nominal blind zone of about 0.75 to 1.25km from the surface (Tanelli et al., 2008) means that a large fraction of Arctic clouds cannot be
275 accurately detected in CloudSat observations. Mech et al. (2019) analysed microwave radar and radiometer measurements near Svalbard during ACLOUD (Wendisch et al., 2019) to find that about 40% of all clouds show cloud tops below 1000 m height, and thus, are likely to be missed by CloudSat. Nomokonova et al. (2019) find a peak frequency of cloud occurrence at 800 to 900 m from Cloudnet observations at Ny Alesund. In the case of ACSE, 50% and 37% of all clouds show cloud tops below 1000 m in summer and autumn, respectively. These numbers increase to 80% and 76% for liquid clouds. About 25% and 41%
280 of mixed-phase clouds are affected during summer and winter, respectively. The effect is smallest for ice clouds with 5% during summer and 14% of observations during autumn.

Figure 9 compares the cloud-fraction profiles derived from the ACSE observations (left panel of Figure 3) to those reported for observations from ASCOS, conducted during August and early September 2008 well within the ice pack in the central

Arctic Ocean. ASCOS cloud fractions were obtained following Shupe (2006). The profiles of total cloud fraction are very
285   similar in shape but show a generally lower cloudiness from ACSE. Note that while the profiles represent roughly the same
period of the year, the actual observations have been performed at different locations and in different years. Nevertheless, the
resemblance in the shape of the total cloud fraction profile indicates the usefulness of relating Arctic observations to each other;
particularly given their scarcity. For the comparison of cloud fraction, we need to keep in mind that the upper measurement
height during ACSE was restricted to 6 km by instrument settings. This constrains all cloud fractions to zero at and above 6 km,
290   as we only consider clouds for which a cloud top has been detected below this height. The total cloud fraction for all clouds
including those with undetected top heights, i.e. top heights above 6 km, is given by the grey dashed line for reference.

The cloud-fraction profile for liquid-only clouds during ACSE generally resembles the profiles derived from ASCOS mea-
surements. However, the occurrence of liquid-only clouds was much lower during ACSE, except for the frequent fog periods in
the lowermost height bins during the summer months. The occurrence of ice and mixed-phase clouds during ACSE also appear
295   to be quite similar to those obtained from ASCOS. Considering that most of the clouds with undetected tops are likely to be ice
clouds and that the shape of the cloud-fraction profile for mixed-phase clouds during ACSE resembles that of ASCOS, Figure
9 shows that the height from which ice clouds are the dominant cloud type was about 1 km lower for ACSE than for ASCOS.

The monthly total cloud fraction of 95% in July, 74% in August and 97% in September as observed during ACSE can also
be put into the context of previous studies. Shupe (2011b) compared observation from surface land sites (Figure 2) in Atqasuk
300   (ceilometer, microwave radiometer), Barrow (ceilometer, radar, micro-pulse lidar, microwave radiometer, Atmospheric Emitted
Radiance Interferometer), Eureka (radar, high spectral resolution lidar, micro-pulse lidar, microwave radiometer, Atmospheric
Emitted Radiance Interferometer), and the SHEBA project (ceilometer, radar, microwave radiometer, Atmospheric Emitted
Radiance Interferometer). For July to September, they present a total cloud fraction of 92% to 98% at Barrow and Sheba.
Lower values of 80% to 85% are given for Atqasuk, while increasing from 65% in July to 80% in August and September
305   at Eureka. Zygmuntowska et al. (2012) and Mioche et al. (2015) used data from the Cloud Profiling Radar (CPR) aboard the
CloudSat satellite (Stephens et al., 2008) and the Cloud-Aerosol Lidar with Orthogonal Polarization (CALIOP) on the Cloud-
Aerosol Lidar and Infrared Pathfinder Satellite Observations (CALIPSO, Winker et al. (2010)) satellite for the years 2007 and
2008, and the period from 2007 to 2010, respectively, to investigate total cloud fraction in the Arctic region. They find consistent
values of 75% to 80% in July, 80% to 87% in August, and 84% to 90% in September. For all clouds, ACSE observations of
310   more than 90% during July and September are mostly in line with the high cloud fractions observed during SHEBA (Shupe,
2011b).

Cloud fractions of 60% to 90% as observed at Eureka (Shupe, 2011b) and for the Arctic region (Zygmuntowska et al., 2012;
Mioche et al., 2015) suggest that the ACSE finding of a total cloud fraction of 74% in August is well within the range of values
one would expect for the Arctic region. However, it should be noted that spaceborne data sets provide better spatial coverage
315   than ground-based measurements during ACSE, and thus, are more representative of average conditions. When comparing the
fraction of mixed-phase clouds observed during ACSE to the multi-year (2007 to 2010) CALIPSO/CloudSat data set analysed
by Mioche et al. (2015) it is apparent that the ground-based ACSE observations during July with a mixed-phase cloud fraction
of 51% are in general agreement with the data from spaceborne instruments. However, ACSE observations of 33% during

August and 80% during September show significantly lower and higher, respectively, fractions of mixed-phase clouds than the
320   satellite record. This is probably the result of natural variability combined with the effect of comparing local measurements
during ACSE to area averaged results from satellite. Considering the fraction of mixed-phase clouds at Barrow, Eureka and
SHEBA (Shupe, 2011b), ACSE findings are in line with SHEBA values of around 50% during July and around 85% during
September. However, the ACSE mixed-phase cloud fraction of 33% during August is much lower than the SHEBA observation
of around 80% (see Figure 2 in Shupe (2011b)). The lower August mixed-phase cloud fraction during ACSE does, however,
325   resemble the findings for Barrow and Eureka (Shupe, 2011b).

Figure 10 compares the connection between the fraction of ice-containing clouds and cloud-top temperature for clouds
observed during ACSE with those reported by Zhang et al. (2010) and Bühl et al. (2013). These previous studies combine
measurements with cloud radar and aerosol lidar from space and ground, respectively. As in this study, they analyse clouds on
a profile-by-profile basis. However, Zhang et al. (2010) and Bühl et al. (2013) focused on mixed-phase clouds at mid-latitudes.
330   While they find that about 50% of all clouds are mixed-phase at a temperature of about -10°C, the ACSE observations reveal
that in the Arctic a mixed-phase cloud fraction of 50% is reached already at -2°C. Previous studies suggest that almost all
non-cirrus clouds with cloud top temperatures below -20°C are mixed-phase at mid-latitudes. In the Arctic, this is the case
already for warmer cloud-top temperatures of -12°C.; though ice-containing cloud fractions for clouds with top temperatures
below -18°C to -25°C were found to be lower than at mid-latitudes for ACSE observations during autumn.
335   Figure 11 puts the ACSE observations of LWP and IWP for clouds during summer and autumn into the context of the earlier
observations of SHEBA and ASCOS. ACSE LWP frequency distributions – though different for summer and autumn – do not
resemble the previous observations, having a wider distribution with less well defined peak. The ACSE observations of IWP
closely follow the ASCOS frequency distribution, although with larger values in the tail. There was quite a substantial part of
the ASCOS ice drift during which mixed-phase stratocumulus clouds dominated, that may bias ASCOS LWP statistics high.
340   In addition, air mass transit time is known to be an important factor in boundary layer structure and hence cloud properties.
The fact that SHEBA and ASCOS have been further away from open water than ACSE means that air mass transit time is a
factor controlling the cloud properties observed.

5   Summary and Conclusions

We present remote-sensing observations of Arctic clouds conducted during a three-month cruise in the Arctic Ocean along the
345   Russian shelf from Tromsø, Norway, to Barrow, Alaska, and back. Observations with ceilometer, Doppler lidar, cloud radar
and microwave radiometer were made within pack ice, open water, and the marginal ice zone. The Cloudnet retrieval has
been applied to investigate cloud properties with special emphasis on the effects of cloud-top temperature and boundary layer
structure. The data set has been split into summer and autumn based on a change in the lower tropospheric mean temperature
observed from radiosoundings (Sotiropoulou et al., 2016).
350   The ACSE data set reveals a strong reduction in the occurrence rate of liquid clouds and an increase for both mixed-phase
clouds and ice clouds at low levels during autumn compared to summer. Ice clouds during autumn extend almost down to the

surface, while low clouds during summer are predominantly liquid. In addition, it was found that liquid clouds vary little in their vertical extent between summer and autumn, while both ice and mixed-phase clouds have lower top and base heights in autumn than in summer.

355 About 74% of all liquid clouds observed during ACSE show LWP below the infra-red black body limit of approximately $50\,\mathrm{g m^{-2}}$. This means that the majority of the observed Arctic liquid water clouds have long-wave radiative properties that are highly sensitive to small changes in LWP. In general, the frequency distribution of LWP shows little variation for mixed-phase and purely liquid clouds. Nevertheless, summer shows more cases of high LWP and fewer cases of low LWP and the mean and median values are higher for mixed-phase clouds. The majority of clouds had an IWP below $20\,\mathrm{g m^{-2}}$ with summer (autumn)
360 mean and median values of 34 and $7\,\mathrm{g m^{-2}}$ (32 and $9\,\mathrm{g m^{-2}}$), respectively.

Whether the PBL structure was coupled or decoupled, and the occurrence of warm air advection had little effect on the geometric thickness of liquid clouds. In contrast, mixed-phase clouds during WAA are generally thinner than for non-WAA. The deepest mixed-phase clouds are found for non-WAA and for decoupled PBLs.

Cloud-top temperatures for all mixed-phase clouds during non-WAA are between 0°C and -30°C. This range is reduced to
365 0°C to -20°C for mixed-phase clouds during WAA.

For liquid water clouds, the normalised profile of LWC reveals a strong increase with height with a maximum between 0.03 and $0.19\,\mathrm{g m^{-3}}$ within the upper quarter of the clouds followed by a sharp decrease towards cloud top. LWC is lowest for clouds observed below the inversion during WAA. Most mixed-phase clouds show a LWC profile with a very similar shape to that of liquid clouds with lower maximum values during WAA than during non-WAA.

370 The normalised profiles of IWC in mixed-phase clouds look different from that of LWC. They show a wider range in maximum values with lowest IWC for clouds below the inversion and highest values for clouds above or extending through the inversion. Note that these correspond to the thinnest and thickest clouds, respectively. The IWC profile generally peaks at a height below the peak in the LWC profile – usually in the centre of the cloud but also closer to cloud base and likely due to more particle sublimation as the crystals fall.

375 Unsurprisingly, it was found that liquid-water clouds during summer show the highest cloud-top temperatures, which can exceed 15°C but don't go below -15°C. As documented in Tjernström et al. (2015, 2019), ACSE cloud-top temperatures above 10°C correspond to a period of strong warm air advection that occurred at the beginning of August 2015. As a consequence, the frequency distribution of cloud-top temperature observed during summer resembles that derived from Cloudnet observations at mid-latitudes (Bühl et al., 2016). In autumn the top temperatures of liquid clouds rarely exceed 0°C with observed values as
380 low as -25°C. The maximum of cloud-top-temperature occurrence rate shifts from 0°C in summer to -5.0°C in autumn.

During summer, the tops of mixed-phase clouds are generally warmer than in autumn with a maximum just below 0°C. However, they are always colder than liquid-only clouds during the same season. During summer, cloud-top temperature can be as low as -25°C though they are mostly warmer than -10°C. Autumn reveals a bi-modal distribution of cloud-top temperature corresponding to precipitating (T_{top} >-10°C) versus non-precipitating clouds (T_{top} <-10°C).

385   The IWC of mixed-phase clouds during summer and autumn mostly feature very low IWC of less than $0.07\,\mathrm{g\,m^{-3}}$, though values exceeding $100\,\mathrm{g\,m^{-3}}$ have been observed during autumn. In general, IWC was lowest in clouds with a low cloud top height and highest for clouds with top heights in the range from 3.0 to 4.0 km.

While the three-month ACSE data set provides comprehensive observations of Arctic clouds, it is challenging to relate the findings to earlier campaigns such as SHEBA or ASCOS. Although we find similar frequency distributions of LWP and IWP,

390   the occurrence rate of clouds during ACSE was lower than during ASCOS. On the one hand, the observations have been conducted in different regions of the Arctic; consequently, observed differences might be the result of regional effects. On the other hand, different campaigns cover different time periods. This means that inter-annual variability might be added on top of potential regional effects – this is particularly highlighted by the warm air advection events observed during ACSE.

Data availability. All data from ACSE are available through the Bolin Centre for Climate Research database (http://www.bolin.su.se).

395   *Author contributions.* PA has analysed the ACSE data set and prepared the manuscript together with IMB and MT. PA has set up the Cloudnet retrieval at Leeds together with EJO. GS has provided the inversion heights from radiosounding. IMB, BJB, GS, MDS, and MT performed the measurements during ACSE. BP has assisted in refining the MWR retrieval for Arctic observations. All authors contributed to the discussion of the results and revision of the manuscript.

Competing interests. The authors declare no competing interests.

400   *Acknowledgements.* ACSE was supported by funding from the Knut and Alice Wallenberg Foundation, Swedish Research Council, Faculty of Science at Stockholm University, US Office of Naval Research, the US National Oceanic and Atmospheric Administration (NOAA), and the UK Natural Environment Research Council (grant No. NE/K011820/1). We are grateful to the Swedish Polar Research Secretariat and to the two captains and crews of the Oden for logistics support. The radiosounding system, Halo lidar, and HATPRO radiometer were supplied by the National Centre for Atmospheric Science (NCAS) Atmospheric Measurement Facility. The cloud radar was provided by NOAA. PA

405   would like to thank Richard Rigby for Linux support while setting up the Cloudnet retrieval.

References

Achtert, P., Brooks, I. M., Brooks, B. J., Moat, B. I., Prytherch, J., Persson, P. O. G., and Tjernström, M.: Measurement of wind profiles by motion-stabilised ship-borne Doppler lidar, Atmos. Meas. Tech., 8, 4993-5007, https://doi.org/10.5194/amt-8-4993-2015, 2015.

Albrecht, B. A., C. W. Fairall, D. W. Thomson, A. B. White, J. B. Snider, and W. H. Schubert, Surface-based remote-sensing of the observed and the adiabatic liquid water-content of stratocumulus clouds. Geophys. Res. Lett., 17, 89-92, 1990

Bennartz, R., Shupe, M.D., Turner, D.D., Walden, V.P., Steffen, K., Cox, C.J., Kulie, M.S., Miller, N.B. and Pettersen, C.: July 2012 Greenland melt extent enhanced by low-level liquid clouds. Nature, 496(7443), pp.83-86. https://doi.org/10.1038/nature12002, 2013.

Birch, C. E., I. M. Brooks, M. Tjernström, S. F. Milton, P. Earnshaw, S. Söderberg, and P. O. G. Persson, The performance of a global and mesoscale model over the central Arctic Ocean during late summer, J. Geophys. Res., 114, https://doi.org/10.1029/2008JD010790, 2009.

Birch, C. E., Brooks, I. M., Tjernström, M., Shupe, M. D., Mauritsen, T., Sedlar, J., Lock, A. P., Earnshaw, P., Persson, P. O. G., Milton, S. F., and Leck, C.: Modelling atmospheric structure, cloud and their response to CCN in the central Arctic: ASCOS case studies, Atmos. Chem. Phys., 12, 3419-3435, https://doi.org/10.5194/acp-12-3419-2012, 2012.

Boeke, R. C., and Taylor, P. C.: Evaluation of the Arctic surface radiation budget in CMIP5 models, J. Geophys. Res. Atmos., 121, 8525–8548, https://doi.org/10.1002/2016JD025099, 2016

Boers, R., Russchenberg, H., Erkelens, J., Venema, V., Van Lammeren, A.C.A.P., Apituley, A. and Jongen, S.C.H.M.: Ground-based remote sensing of stratocumulus properties during CLARA, 1996, J. Appl. Meteorol., 39(2), 169-181, https://doi.org/10.1175/1520-0450(2000)039<0169:GBRSOS>2.0.CO;2, 2000.

Brooks, M. E., Hogan, R. J., and Illingworth, A. J.: Parameterizing the Difference in Cloud Fraction Defined by Area and by Volume as Observed with Radar and Lidar, J. Atmos. Sci., https://doi.org/ 10.1175/JAS3467.1, 2005

Brooks, I. M., M. Tjernström, P. O. G. Persson, M. Shupe, R. A. Atkinson, G. Canut , C. E. Birch, T. Mauritsen, J. Sedlar, B. J. Brooks: The vertical turbulent structure of the Arctic summer boundary layer during ASCOS, J. Geophys. Res. 122, https://doi.org/10.1002/2017JD027234, 2017.

Bühl, J., A. Ansmann, P. Seifert, H. Baars, and R. Engelmann: Towards a quantitative characterization of heterogeneous ice formation with lidar/radar: Comparison of CALIPSO/CloudSat with ground-based observations, Geophys. Res. Lett., 40, 4404–4408, https://doi.org/10.1002/grl.50792, 2013.

Bühl, J., Seifert, P., Myagkov, A., and Ansmann, A.: Measuring ice- and liquid-water properties in mixed-phase cloud layers at the Leipzig Cloudnet station, Atmos. Chem. Phys., 16, 10609-10620, https://doi.org/10.5194/acp-16-10609-2016, 2016.

Choi, Y.-S., C.-H. Ho, C.-E. Park, T. Storelvmo, and I. Tan: Influence of cloud phase composition on climate feedbacks, J. Geophys. Res. Atmos., 119, 3687–3700, https://doi.org/10.1002/2013JD020582, 2014.

Crewell, S., and Löhnert, U., Accuracy of cloud liquid water path from ground-based microwave radiometry 2. Sensor accuracy and synergy, Radio Sci., 38, 8042, https://doi.org/10.1029/2002RS002634, 2003)

Ebell, K., U. Löhnert, S. Crewell and D. D. Turner, On characterizing the error in a remotely sensed liquid water content profile, Atmos. Res., 98, 57-68, https://doi.org/10.1016/j.atmosres.2010.06.002, 2010.

Ebell, K., Nomokonova, T., Maturilli, M., and Ritter, C.: Radiative effect of clouds at Ny-Ålesund, Svalbard, as inferred from ground-based remote sensing observations, J. Appl. Meteor. Climatol., 59, https://doi.org/10.1175/JAMC-D-19-0080.1, 2020.

Hines, K. M. and Bromwich, D. H.: Simulation of Late Summer Arctic Clouds during ASCOS with Polar WRF, Mon. Wea. Rev., 145, 521-541, https://doi.org/10.1175/MWR-D-16-0079.1, 2017.

Hogan, R.J., Mittermaier, M.P. and Illingworth, A.J., The retrieval of ice water content from radar reflectivity factor and temperature and its use in evaluating a mesoscale model, J. Appl. Meteorol. Climatol., 45(2), 301-317, https://doi.org/10.1175/JAM2340.1, 2006.

445 Illingworth, A.J., Hogan, R.J., O'Connor, E.J., Bouniol, D. and et al., Cloudnet. B. Am. Meteorol. Soc., 88, p.883., 2007.

Karlsson, J. and Svensson, The simulation of Arctic clouds and their influence on the winter surface temperature in present-day climate in the CMIP3 multi-model dataset , G. Clim Dyn, 36: 623. https://doi.org/10.1007/s00382-010-0758-6, 2011.

Komurcu, M., T. Storelvmo, I. Tan, U. Lohmann, Y. Yun, J. E. Penner, Y. Wang, X. Liu, and T. Takemura, Intercomparison of the cloud water phase among global climate models, J. Geophys. Res. Atmos., 119, 3372–3400, https://doi.org/10.1002/2013JD021119, 2014.

450 Liu, Y., J. R. Key, Z. Liu, and X. Wang, and S. J. Vavrus, A cloudier Arctic expected with diminishing sea ice, Geophys. Res. Lett., 39, L05705, https://doi.org/10.1029/2012GL051251, 2012.

Löhnert, U. and Crewell, S.: Accuracy of cloud liquid water path from ground-based microwave radiometry. 1. Dependency on cloud model statistics, Radio Sci., 38, 8041, https://doi.org/10.1002/2002RS002654, 2003.

Manninen, A. J., E. J. O'Connor, V. Vakkari, and T. Petäjä, A generalised background correction algorithm for a Halo Doppler lidar and its
455 application to data from Finland, Atmos. Meas. Tech., 9, 817-827, https://doi.org/10.5194/amt-9-817-2016, 2016.

Markus, T., J. C. Stroeve, and J. Miller, Recent changes in Arctic sea ice melt onset, freezeup, and melt season length, J. Geophys. Res., 114, https://doi.org/10.1029/2009JC005436, 2009.

Maslanik, J., J. Stroeve, C. Fowler, and W. Emery, Distribution and trends in Arctic sea ice age through spring 2011, Geophys. Res. Lett., 38, https://doi.org/10.1029/2011GL047735, 2011.

460 Massaro G., I. Stiperski, B. Pospichal, and M. W. Rotach, Accuracy of retrieving temperature and humidity profiles by ground-based microwave radiometry in truly complex terrain, Atmos. Meas. Tech (2015), 8, 3355-3367, https://doi.org/ 10.5194/amt-8-3355-2015, 2015.

Markus, T., J. C. Stroeve, and J. Miller, Recent changes in Arctic sea ice melt onset, freezeup, and melt season length, J. Geophys. Res., 114, https://doi.org/10.1029/2009JC005436, 2009.

Mauritsen, T., Sedlar, J., Tjernström, M., Leck, C., Martin, M., Shupe, M., Sjogren, S., Sierau, B., Persson, P. O. G., Brooks, I. M., and
465 Swietlicki, E., An Arctic CCN-limited cloud-aerosol regime, Atmos. Chem. Phys., 11, 165-173, https://doi.org/10.5194/acp-11-165-2011, 2011.

Mech, M., Kliesch, L.-L., Anhäuser, A., Rose, T., Kollias, P., and Crewell, S.: Microwave Radar/radiometer for Arctic Clouds (MiRAC): first insights from the ACLOUD campaign, Atmos. Meas. Tech., 12, 5019–5037, https://doi.org/10.5194/amt-12-5019-2019, 2019.

Mioche, G., O. Jourdan, M. Ceccaldi, and J. Delanoë, Variability of mixed-phase clouds in the Arctic with a focus on the Svalbard region: a
470 study based on spaceborne active remote sensing, Atmos. Chem. Phys., 15, 2445-2461, https://doi.org/10.5194/acp-15-2445-2015, 2015.

Moran, K. P., S. Pezoa, C. W. Fairall, C. R. Williams, T. E. Ayers, A. Brewer, S. P. de Szoeke, and V. Ghate, A motion stabilized W-band radar for shipboard observations of marine boundary-layer clouds. Bound.-Layer Meteor., 143, 3–24, https://doi.org/10.1007/s10546-011-9674-5, 2012.

Nomokonova, T., Ebell, K., Löhnert, U., Maturilli, M., Ritter, C., and O'Connor, E.: Statistics on clouds and their relation to thermodynamic
475 conditions at Ny-Ålesund using ground-based sensor synergy, Atmos. Chem. Phys., 19, 4105–4126, https://doi.org/10.5194/acp-19-4105-2019, 2019.

Polyakov, I. V., Alekseev, G. V., Bekryaev, R. V., Bhatt, U., Colony, R., Johnson, M. A., Karklin, V. P., Makshtas, A. P.,Walsh, D., and Yulin, A. V., Observationally based assessment of polar amplification of global warming, Geophys. Res. Lett. 29, 1878, https://doi.org/1029/2001GL011111, 2002.

480   Sedlar, J. and Tjernström, M., Stratiform cloud—Inversion characterization during the Arctic melt season. Boundary-layer meteorology, 132(3), pp.455-474, 2009.

Sedlar, J., Tjernström, M., Mauritsen, T., Shupe, M.D., Brooks, I.M., Persson, P.O.G., Birch, C.E., Leck, C., Sirevaag, A. and Nicolaus, M., A transitioning Arctic surface energy budget: the impacts of solar zenith angle, surface albedo and cloud radiative forcing, Climate dynamics, 37(7-8), 1643-1660, 2011.

485   Sedlar, J., Shupe, M.D. and Tjernström, M., On the relationship between thermodynamic structure and cloud top, and its climate significance in the Arctic. J. Clim., 25, 2374-2393, 2012.

Serreze, M. C., and Francis, J. A., The Arctic amplification debate, Clim. Change, 76, 241–264, https://doi.org/ 10.1007/s10584-005-9017-y, 2006.

Serreze, M. C., and Barry, R. G., Processes and impacts of Arctic amplification: A research synthesis. Global and Planetary Change 77,
490   85–96, https://doi.org/10.1016/j.gloplacha.2011.03.004, 2011

Shupe, M.D., and J.M. Intrieri, Cloud radiative forcing of the Arctic surface: The influence of cloud properties, surface albedo, and solar zenith angle, J. Climate, 17, 616-628, 2004.

Shupe, M.D., S.Y. Matrosov, and T. Uttal, Arctic mixed-phase cloud properties derived from surface-based sensors at SHEBA. J. Atmos. Sci., 63, 697-711, 2006.

495   Shupe, M. D., A ground-based multisensor cloud phase classifier, Geophys. Res. Lett., 34, L22809, https://doi.org/10.1029/2007GL031008, 2007.

Shupe, M.D., Walden, V.P., Eloranta, E., Uttal, T., Campbell, J.R., Starkweather, S.M. and Shiobara, M., Clouds at Arctic atmospheric observatories. Part I: Occurrence and macrophysical properties. J. Appl. Meteorol. Clim., 50, 626-644, 2011a.

Shupe, M. D., 2011b: Clouds at Arctic atmospheric observatories. Part II: Thermodynamic phase characteristics. J. Appl. Meteor. Climatol.,
500   50, 645–661.

Shupe, M. D., P. O. G. Persson, I. M. Brooks, M. Tjernström, J. Sedlar, T. Mauritsen, C. Leck, S. Sjogren, Cloud and boundary layer interactions over the Arctic sea-ice in late summer, Atmos. Chem. Phys. 13, 9379–9400, https://doi.org/10.5194/acp-13-9379-2013, 2013.

Sotiropoulou, G., J. Sedlar, M. Tjernström, M. Shupe, I. M. Brooks, P. O. G. Persson, The thermodynamic structure of summer Arctic stratocumulus and the dynamic coupling to the surface. Atmos. Chem. Phys., 14, 12573–12592, https://doi.org/10.5194/acp-14-12573-
505   2014, 2014.

Sotiropoulou, G., Tjernström, M., Sedlar, J., Achtert, P., Brooks, B. J., Brooks, I. M., Persson, P. O. G., Prytherch, J., Salisbury, D. J., Shupe, M. D. and Johnston, P. E., Atmospheric Conditions during the Arctic Clouds in Summer Experiment (ACSE): Contrasting Open Water and Sea Ice Surfaces during Melt and Freeze-Up Seasons. J. Clim., 29, 8721-8744, 2016.

Steele, M., J. Zhang, and W. Ermold, Mechanisms of summertime upper Arctic Ocean warming and the effect on sea ice melt, J. Geophys.
510   Res., 115, https://doi.org/10.1029/2009JC005849, 2010.

Stephens, G.L., Vane, D.G., Tanelli, S., Im, E., Durden, S., Rokey, M., Reinke, D., Partain, P., Mace, G.G., Austin, R. and L'Ecuyer, T.: CloudSat mission: Performance and early science after the first year of operation. J. Geophys. Res. – Atmos., 113(D8), 2008.

Solomon, A., Morrison, H., Persson, O., Shupe, M.D. and Bao, J.W., Investigation of microphysical parameterizations of snow and ice in Arctic clouds during M-PACE through model–observation comparisons. Monthly Weather Review, 137, 3110-3128, 2009.

515   Solomon, A., M. D. Shupe, P.O.G. Persson, and H. Morrison, Moisture and dynamical interactions maintaining decoupled Arctic mixed-phase stratocumulus in the presence of a humidity inversion. Atmos. Chem. Phys., 11, 10127-10148, https://doi.org/10.5194/acp-11-10127-2011, 2011.

Stocker (2014), ed. Climate change 2013: the physical science basis, Cambridge University Press.

Stroeve, J. C., V. Kattsov, A. Barrett, M. Serreze, T. Pavlova, M. Holland, and W. N. Meier, Trends in Arctic sea ice extent from CMIP5,
520   CMIP3 and observations, Geophys. Res. Lett., 39, L16502, https://doi.org/10.1029/2012GL052676, 2012.

Tan, I., Storelvmo, T. and Zelinka, M.D., Observational constraints on mixed-phase clouds imply higher climate sensitivity. Science,
352(6282), pp.224-227, 2016.

Tanelli, S., Durden, S. L., Im, E., Pak, K. S., Reinke, D. G., Partain, P., Haynes, J. M., and Marchand, R. T.: CloudSat's cloud
profiling radar after two years in orbit: Performance, calibration, and processing, IEEE T. Geoscience Remote, 46, 3560–3573,
525   https://doi.org/10.1109/TGRS.2008.2002030, 2008.

Tjernström, M., The summer Arctic boundary layer during the Arctic Ocean Experiment 2001 (AOE-2001), Bound.-Layer Meteorol., 117,
5–36, 2005.

Tjernström, M., Sedlar, J. and Shupe, M.D., How well do regional climate models reproduce radiation and clouds in the Arctic? An evaluation
of ARCMIP simulations. Journal of Applied Meteorology and Climatology, 47(9), pp.2405-2422, 2008.

530   Tjernström, M., and R. G. Graversen, The vertical structure of the lower Arctic troposphere analysed from observations and the ERA- 40
reanalysis. Quart. J. Roy. Meteor. Soc., 135, 431–443, https://doi.org/10.1002/qj.380, 2009.

Tjernström, M., Birch, C. E., Brooks, I. M., Shupe, M. D., Persson, P. O. G., Sedlar, J., Mauritsen, T., Leck, C., Paatero, J., Szczodrak, M.,
and Wheeler, C. R.: Meteorological conditions in the central Arctic summer during the Arctic Summer Cloud Ocean Study (ASCOS),
Atmos. Chem. Phys., 12, 6863–6889, https://doi.org/10.5194/acp-12-6863-2012, 2012.

535   Tjernström, M., Leck, C., Birch, C. E., Bottenheim, J. W., Brooks, B. J., Brooks, I. M., Bäcklin, L., Chang, R. Y.-W., de Leeuw, G., Di
Liberto, L., de la Rosa, S., Granath, E., Graus, M., Hansel, A., Heintzenberg, J., Held, A., Hind, A., Johnston, P., Knulst, J., Martin, M.,
Matrai, P. A., Mauritsen, T., Müller, M., Norris, S. J., Orellana, M. V., Orsini, D. A., Paatero, J., Persson, P. O. G., Gao, Q., Rauschenberg,
C., Ristovski, Z., Sedlar, J., Shupe, M. D., Sierau, B., Sirevaag, A., Sjogren, S., Stetzer, O., Swietlicki, E., Szczodrak, M., Vaattovaara, P.,
Wahlberg, N., Westberg, M., and Wheeler, C. R.: The Arctic Summer Cloud Ocean Study (ASCOS): overview and experimental design,
540   Atmos. Chem. Phys., 14, 2823-2869, https://doi.org/10.5194/acp-14-2823-2014, 2014.

Tjernström, M., Shupe, M. D., Brooks, I. M., Persson, P. O. G., Prytherch, J., Salisbury, D. J., Sedlar, J., Achtert, P., Brooks, B.J., Johnston,
P. E. and Sotiropoulou, G.: Warm-air advection, air mass transformation and fog causes rapid ice melt, Geophys. Res. Lett., 42, pp.5594-
5602, 2015.

Tjernström, M., Shupe, M. D., Prytherch, J., Achtert, P., Brooks, I. M., and Sedlar, J.: Arctic summer air-mass transformation, surface
545   inversions and the surface energy budget, J. Clim, https://doi.org/10.1175/JCLI-D-18-0216.1, 2019.

Turner, D. D.: Improved ground-based liquid water path retrievals using a combined infrared and microwave approach, J. Geophys. Res.,
112, D15204, https://doi.org/10.1029/2007JD008530, 2007.

Uttal, T., Curry, J. A., Mcphee, M. G., Perovich, D. K., Moritz, R. E., Maslanik, J. A., Guest, P. S., Stern, H. L., Moore, J. A., Turenne, R.,
Heiberg, A., Serreze, M. C., Wylie, D. P., Persson, P. O. G., Paulson, C. A., Halle, C., Morison, J. H., Wheeler, P. A., Makshtas, A., Welch,
550   H., Shupe, M. D., Intrieri, J. M., Stamnes, K., Lindsey, R.W., Pinkel, R., Pegau,W. S., Stanton, T. P., and Grenfeld, T. C.: Surface Heat
Budget of the Arctic Ocean, B. Am. Meteorol. Soc., 83, 255–276, 2002.

Wendisch, M., A. Macke, A. Ehrlich, C. Lüpkes, M. Mech, D. Chechin, K. Dethloff, C. Barientos, H. Bozem, M. Brückner, H. Clemen,
S. Crewell, T. Donth, R. Dupuy, K. Ebell, U. Egerer, R. Engelmann, C. Engler, O. Eppers, M. Gehrmann, X. Gong, M. Gottschalk, C.
Gourbeyre, H. Griesche, J. Hartmann, M. Hartmann, B. Heinold, A. Herber, H. Herrmann, G. Heygster, P. Hoor, S. Jafariserajehlou,
555   E. Jäkel, E. Järvinen, O. Jourdan, U. Kästner ,S. Kecorius, E. Knudsen, F. Köllner, J. Kretzschmar, L. Lelli, D. Leroy, M. Maturilli, L.

Mei, S. Mertes, G. Mioche, R. Neuber, M. Nicolaus, T. Nomokonova, J. Notholt, M. Palm, M. van Pinxteren, J. Quaas, P. Richter, E. Ruiz-Donoso, M. Schäfer, K. Schmieder, M. Schnaiter, J. Schneider, A. Schwarzenböck, P. Seifert, M. Shupe, H. Siebert, G. Spreen, J. Stapf, F. Stratmann, T. Vogl, A. Welti, H. Wex, A. Wiedensohler, M. Zanatta, and S. Zeppenfeld: The Arctic Cloud Puzzle: Using ACLOUD/PASCAL Multi-Platform Observations to Unravel the Role of Clouds and Aerosol Particles in Arctic Amplification. Bull. Amer. Meteor. Soc., https://doi.org/10.1175/BAMS-D-18-0072.1, 2019.

Westbrook, C.D. and Illingworth, A.J.: Evidence that ice forms primarily in supercooled liquid clouds at temperatures >- 27 C, Geophys. Res. Lett., 38, https://doi.org/10.1029/2011GL048021, 2011.

Winker, D.M., Pelon, J., Coakley Jr, J.A., Ackerman, S.A., Charlson, R.J., Colarco, P.R., Flamant, P., Fu, Q., Hoff, R.M., Kittaka, C. and Kubar, T.L.: The CALIPSO mission: A global 3D view of aerosols and clouds. Bull. Am. Meteorol. Soc., 91, pp.1211-1229, 2010.

Walsh, J.E., Chapman, W.L. and Portis, D.H.: Arctic cloud fraction and radiative fluxes in atmospheric reanalyses, J. Clim., 22, pp.2316-2334, 2009.

Zhang, D., Wang, Z., and Liu, D.: A global view of midlevel liquid-layer topped stratiform cloud distribution and phase partition from CALIPSO and CloudSat measurements, J. Geophys. Res., 115, https://doi.org/10.1029/2009JD012143, 2010.

Zygmuntowska, M., Mauritsen, T., Quaas, J., and Kaleschke, L.: Arctic Clouds and Surface Radiation – a critical comparison of satellite retrievals and the ERA-Interim reanalysis, Atmos. Chem. Phys., 12, 6667–6677, https://doi.org/10.5194/acp-12-6667-2012, 2012.
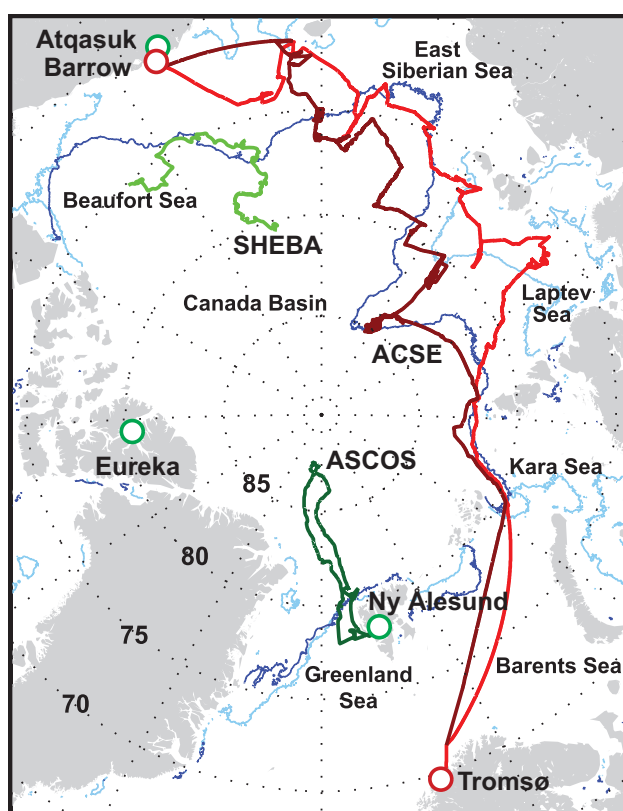
Figure 1. Map of the ACSE cruise track (leg 1 in red, leg 2 in burgundy) together with the sea ice extent on 5 July 2014 (light blue) and 5 October 2014 (dark blue). The tracks of the ASCOS and SHEBA experiments are given in dark and light green, respectively. Red circles mark the start and end of the ACSE cruise track. Green circles give the location of other Arctic sites referred to in this paper.
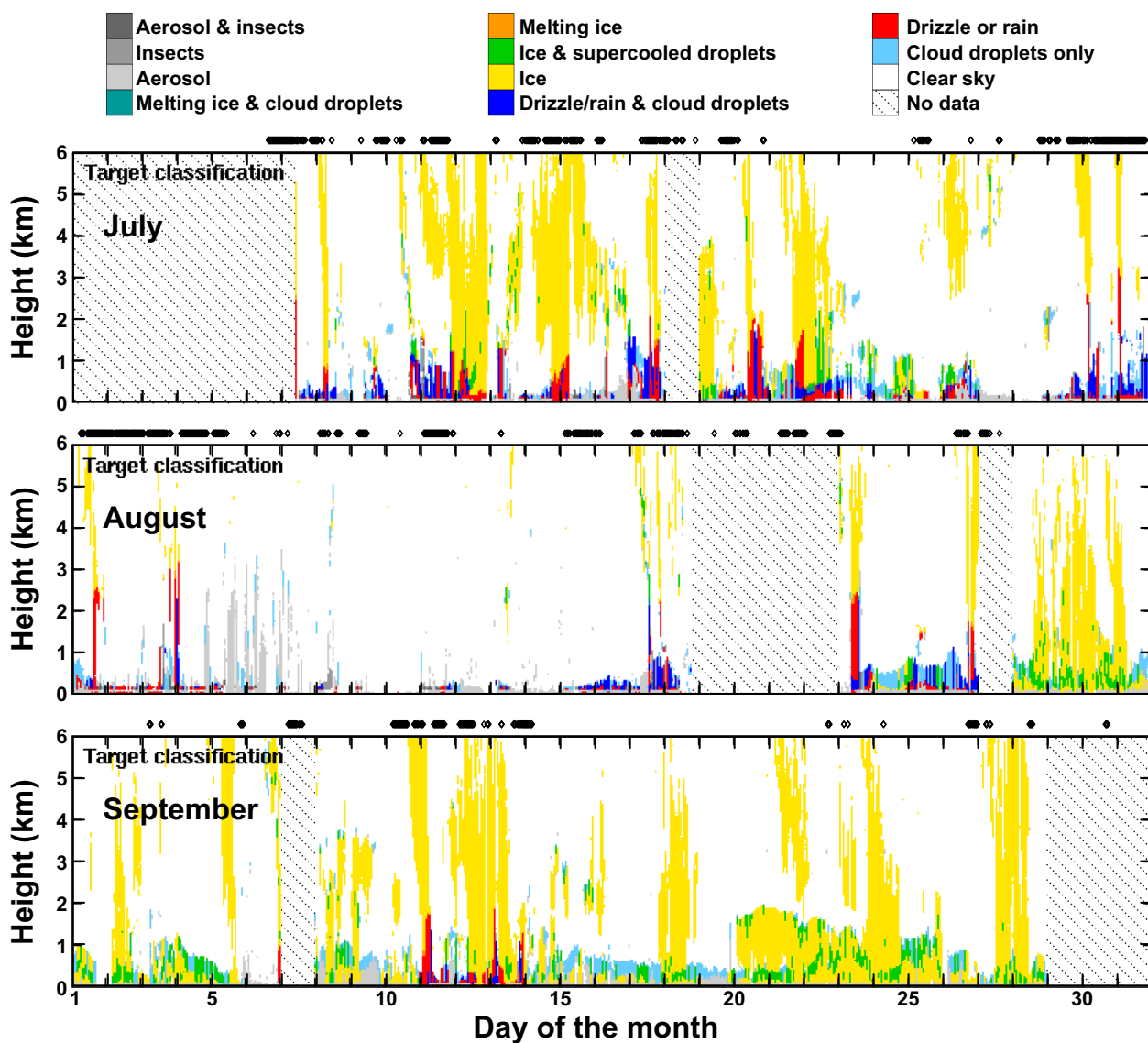
Figure 2. Cloudnet target classification for the three-month ACSE cruise. Black diamonds above the monthly displays mark 10-min periods of visibility below 1 km. Hatched areas separate periods of no data from the white background of *Clear sky*.
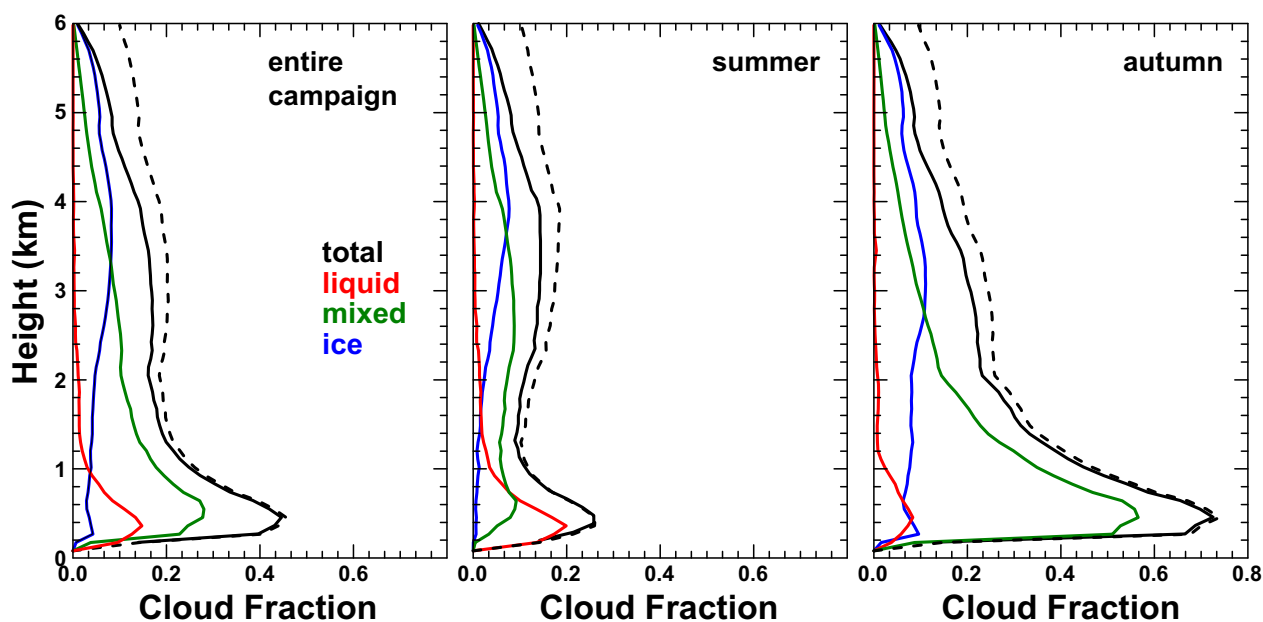
Figure 3. Profiles of cloud fraction for different cloud types as obtained using Cloudnet for the entire ACSE campaign (left), summer (middle), and autumn (right). All solid profiles refer to clouds for which the cloud-top height was located below 6 km height. The dashed lines refer to the total cloud fraction with respect to all clouds, i.e. including those with undetected cloud-top heights.
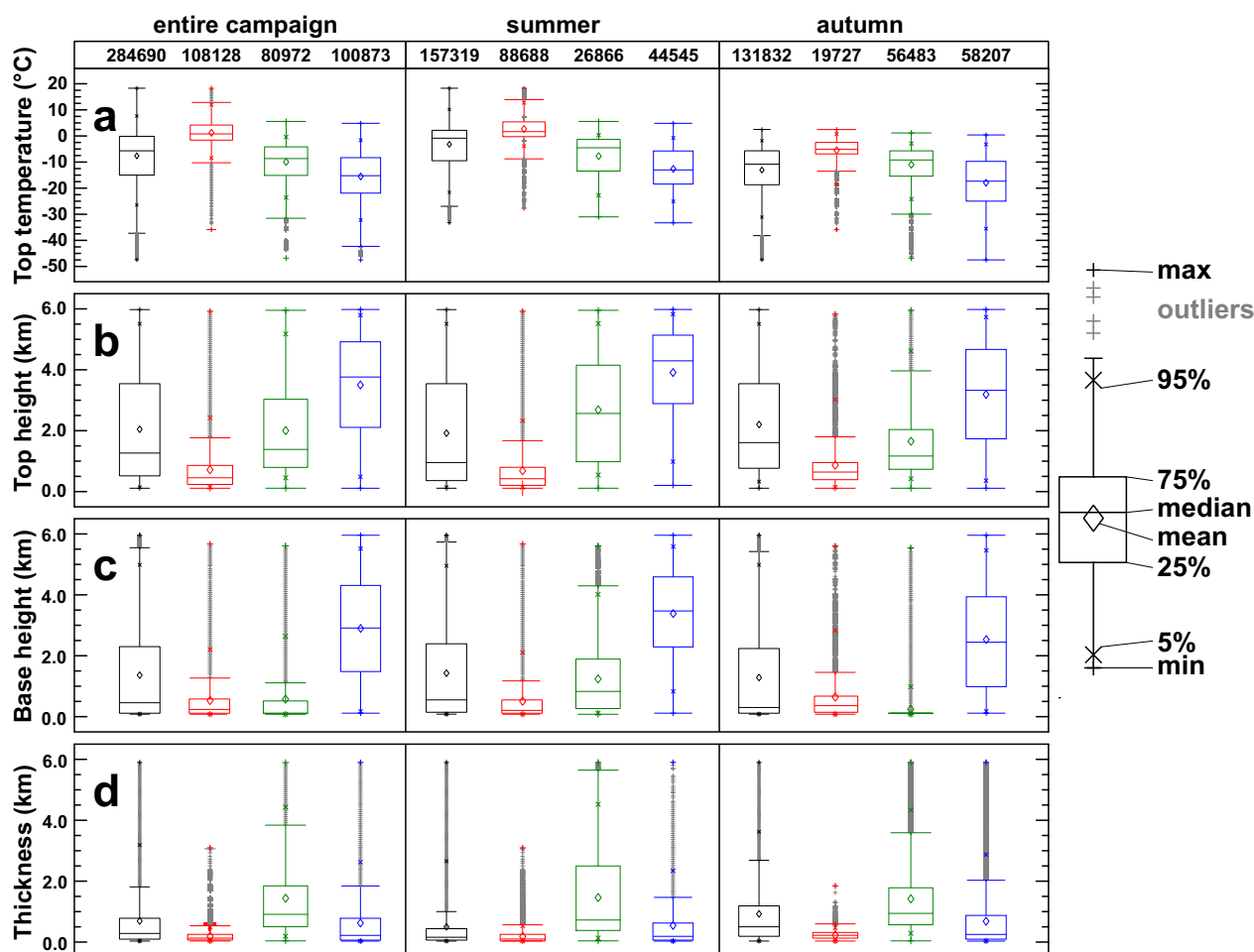
Figure 4. Statistical overview of cloud occurrence with respect to (a) top temperature, (b) top height, (c) base height, and (d) geometrical thickness for the entire ACSE campaign (left column) as well as for summer (middle column) and autumn (right column). The colours indicate the different cloud types as in Figure 3. The numbers in the top panel refer to the number of 30-s profiles considered in the analysis.
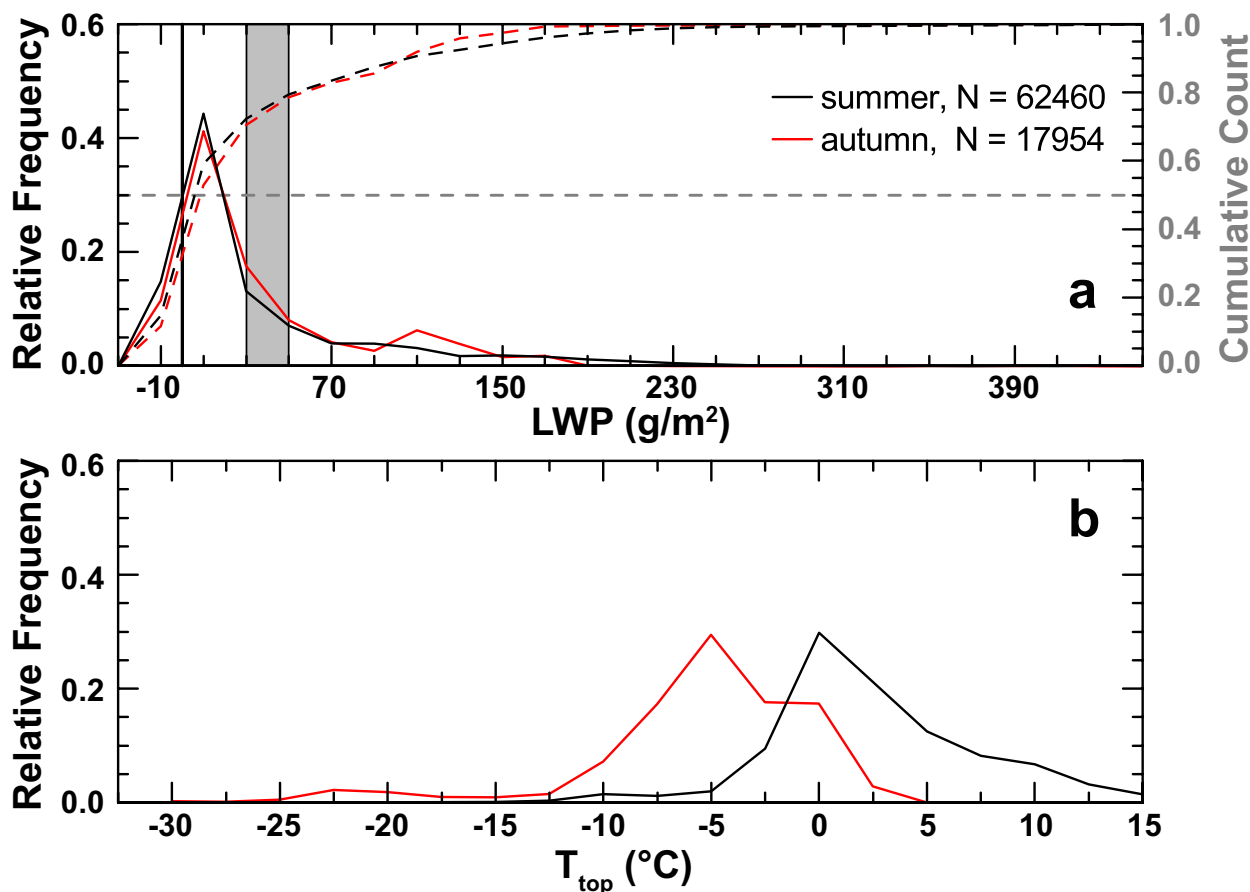
Figure 5. (a) Histogram (solid lines) and cumulative count (dashed lines) of the occurrence frequency of liquid water path, and (b) histogram of the cloud top temperature for liquid clouds observed during summer (black) and autumn (red). Values represent individual cloud layers on a profile basis. The grey dashed line in (a) marks 50% in the cumulative counts. The vertical line in (a) marks $0\,\mathrm{g\,m^{-2}}$ LWP while the grey area indicates the infrared black body limit between 30 and $50\,\mathrm{g\,m^{-2}}$ LWP.
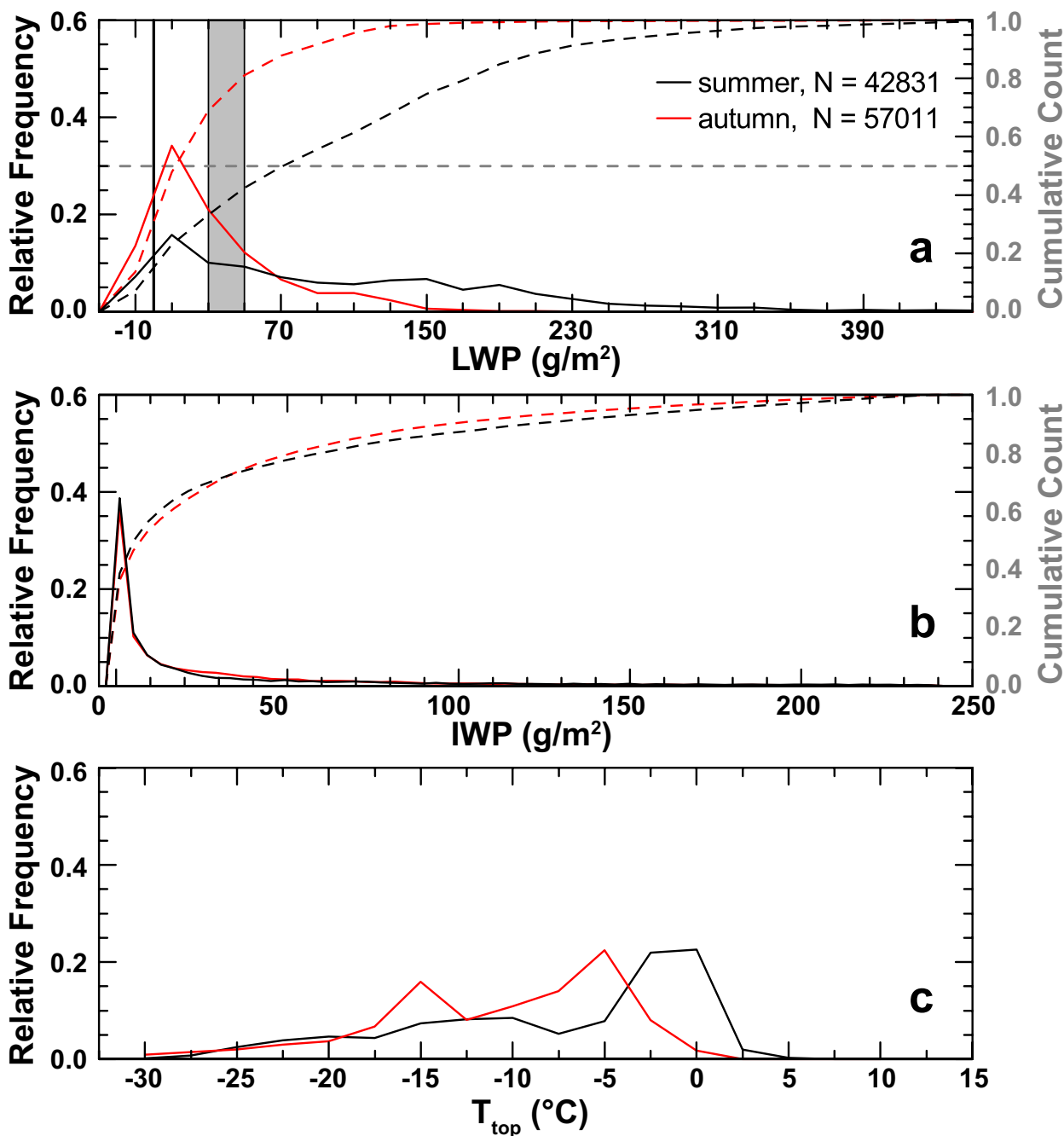
Figure 6. Histogram (solid lines) and cumulative count (dashed lines) of the occurrence frequency of liquid water path, ice water path as well as the histogram of the cloud top temperature for mixed-phase clouds observed during summer (black) and autumn (red). Values give the number of considered cloud layers as observed on a profile basis. The grey dashed line in (a) marks 50% in the cumulative counts. The vertical lines in (a) mark 0 and $50\,\mathrm{g\,m^{-2}}$ LWP. The latter is the infrared black body limit.
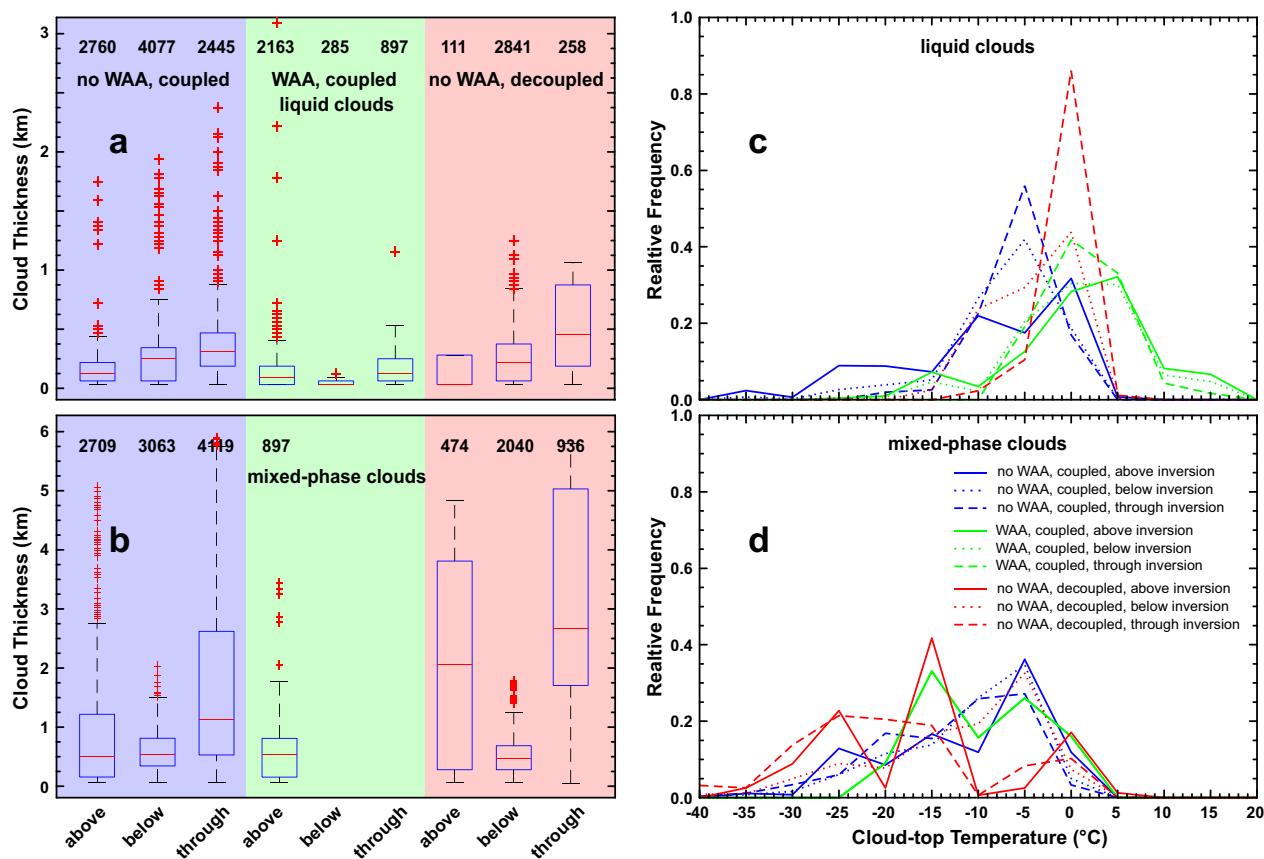
Figure 7. Statistics on the geometrical thickness (a and b) and the frequency distribution of cloud-top-temperature (c and d) of liquid (a and c) and mixed-phase (b and d) clouds observed for different PBL structure and large-scale circulation: non-WAA with coupled PBL (blue), non-WAA with decoupled PBL (red), and WAA with coupled PBL (green). The different boxes (a and b) and lines in (c and d) refer to clouds with cloud base above the inversion (above), to clouds with cloud top below the inversion (below) or to clouds with cloud base below the inversion and cloud top above the inversion (through). Numbers in (a) and (b) refer to the number of Cloudnet profiles per category. Categories with less than 100 profiles have been omitted; this includes all cases of decoupled PBL during WAA.
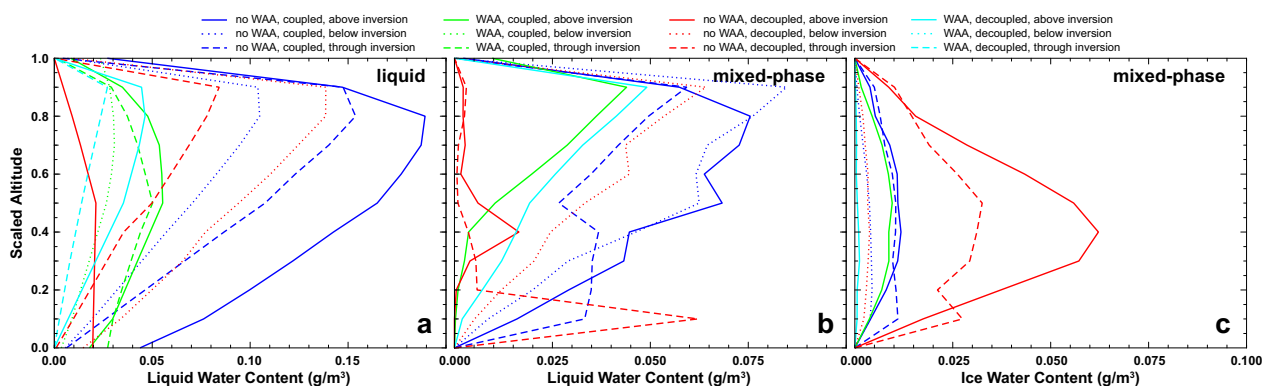
Figure 8. Scaled profiles of LWC (a, b) and IWC (c) of liquid and mixed-phase clouds observed for different PBL structure, large-scale circulation, and location with respect to the main inversion. Zero and unity of the scaled altitude refer to cloud base and top, respectively. Categories with less than 100 profiles have not been included.
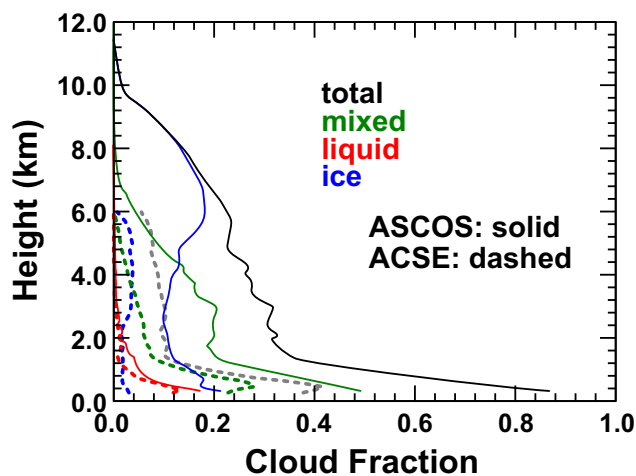
Figure 9. Profiles of cloud fraction for different cloud types as derived from measurements during ASCOS (solid, 12 August to 2 September 2008) and ACSE (dashed) for the ASCOS time period. The grey dashed lines refers to all clouds, i.e. including those for which cloud top extended above the maximum measurement range of 6 km height.
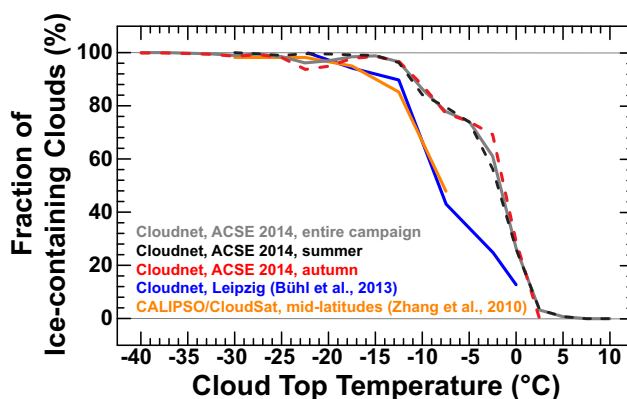
Figure 10. Fraction of mixed-phase clouds observed during ACSE in summer (black) and autumn (red) in comparison to previous observations of mid-level clouds at mid-latitudes from ground (Bühl et al., 2013) and space (Zhang et al., 2010).
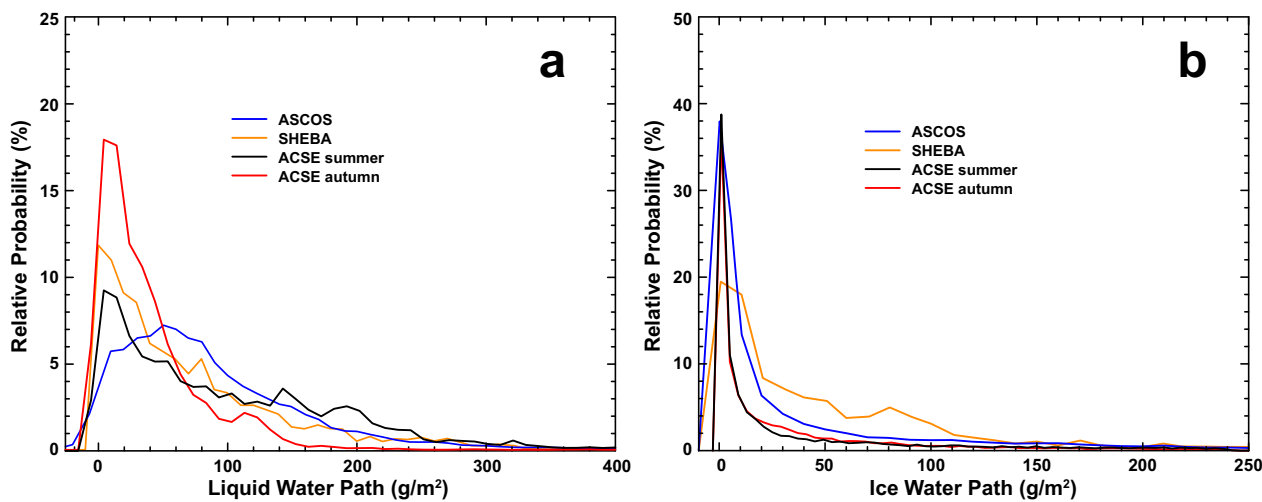
Figure 11. Relative probability of (a) LWP and (b) IWP for mixed-phase clouds observed during ACSE in summer (black) and autumn (red) in comparison to previous observations during ASCOS (blue) and SHEBA (orange). Figure adapted from Figure 17 in Tjernström et al. (2012).